MDPI

Article

Simplifying UAV-based photogrammetry in forestry: how to generate accurate Digital Terrain Model and assess flight mission settings

Facundo Pessacg [1], Francisco Gómez-Fernández [1], Matías Nitsche [1], Nicolás Chamo [1], Sebastián Torrella [2] Rubén Ginzburg [2] and Pablo De Cristóforis [1,*]

[1] Instituto en Ciencias de la Computación (UBA-CONICET), Argentina
[2] Departamento de Ecología, Genética y Evolución, Facultad de Ciencias Exactas y Naturales, Universidad de Buenos Aires, and IEGEBA (UBA–CONICET), Argentina
* Correspondence: pdecris@dc.uba.ar

Abstract: In forestry, aerial photogrammetry by means of Unmanned Aerial Systems (UAS) could bridge the gap between detailed fieldwork and broad-range satellite imagery-based analysis. However, optical sensors are only poorly capable of penetrating the tree canopy, causing raw image-based point clouds unable to reliably collect and classify ground points in woodlands which is essential for further data processing. In this work, we propose a novel method to overcome this issue and generate accurate Digital Terrain Model (DTM) in forested environments by processing the point cloud. We also developed a highly realistic custom simulator that allows controlled experimentation with repeatability guaranteed. With this tool, we performed an exhaustive evaluation of the survey and sensor settings and their impact on the 3D reconstruction. Overall, we found that a high frontal overlap (95%), a nadir camera angle (90°) and low flight altitudes (less than 100m) results in the best configuration for forest environments. We validated the presented method for DTM generation in simulated and real-world survey missions with both fixed-wing and multicopter UAS, showing how the problem of structural forest parameters estimation can be better addressed. Finally, we applied our method for automatic detection of selective logging.

Keywords: Aerial photogrammetry; digital terrain model; structural forest parameters; unmanned aerial systems

Citation: Pessacg, F.; Gómez-Fernández, F.; Nitsche, M.; Chamo,N.; Torrella, S.; Ginzburg R.; De Cristóforis, P. Simplifying UAV-based photogrammetry in forestry: how to generate accurate Digital Terrain Model and assess flight mission settings. *Forests* **2021**, *1*, 0. https://doi.org/

Received:
Accepted:
Published:

1. Introduction

The use of Unmanned Aerial Systems (UAS) as remote sensing for environmental monitoring and precision forestry has grown considerably during last years and become world widespread [1–3]. It has emerged as a promising alternative to satellite imagery and fieldwork. Satellite imagery and vegetation indices obtained from these are useful for land and forest monitoring at the regional level, but not at a predial scale. Fieldwork provides highly detailed information, but it does not scale in terms of cost-area ratio and carries potential risks for the personnel involved. Contrariwise, UAS present several advantages such as the possibility of performing precise full-coverage forest maps in a short time, arbitrary revisit lapse, high spatial resolution, cloudiness independence, low cost, and easy operation compare with its counterparts [4].

Regarding the sensory system, it can be differentiated between two types of UAS depending on whether they use laser scanner or imaging camera as main sensor. At present, airborne laser scanning (ALS) is considered the most accurate method for estimating forest structure due to the detection of both the canopy and the ground. Despite that, ALS systems have considerable power requirements, and they are expensive compared to cameras-based systems and only cost-effective in large scale applications [5,6]. On the other hand, aerial photogrammetry using standard cameras has a better trade-off between cost and performance with respect to forest structure analysis, and it is lightweight

and energy efficient [6]. Aerial photogrammetry is attractive for forestry due its ability to use uncalibrated cameras paired with unstable or handheld platforms, enabling the use of low-cost and off-the-shelf equipment, as mentioned in [7]. Aerial photogrammetry by means of UAS has been employed for tree health monitoring [8–10], 3D model reconstruction [11], species classification [12] and biodiversity assessments [13]. A review of recent advances in forest applications using UAS can be found in [14]. For comparison between laser scanners methods and aerial photogrammetry refer to [15–17].

The photogrammetry workflow can be roughly divided in five main steps: 1) imagery acquisition; 2) keypoint identification between images; 3) camera parameters estimation and sparse point cloud generation using Structure from Motion (SfM); 4) creation of a dense 3D point cloud using multi view stereo (MVS) matching algorithms; and finally 5) post-processing of the 3D cloud.

For step 1) a survey mission needs to be prepared, that involves the generation of a flight plan covering the area of interest where airborne images will be acquired. Depending on the chosen platform type and the expected reconstruction precision, mission settings are chosen. This is usually a manual process which ultimately falls into the hands of expert UAS pilots since there are no standardized protocols yet.

Steps 2), 3) and 4) are generally solved using dedicated software, such as the open source system OpenDroneMap (ODM)[1] or the commercial software Agisoft Metashape[2]. ODM used together with WebODM (a web-based interface to ODM) allows to perform automatic reconstructions on a server where is hosted. It can be used by non-experts users. In contrast, Agisoft Metashape processes images in a semi-automatic sequential approach. This scheme has the advantage that it is easy to detect the source of reconstruction errors, but it requires technical knowledge to obtain the expected results.

Subsequent post-processing steps of the 3D cloud typically involve the estimation of a Digital Surface Model (DSM) and an orthomosaic. In forestry, it is also required to generate a Canopy Height Model (CHM), normalizing the DSM, by means of translating from height above sea level to height above ground, based on a generated or preexisting Digital Terrain Model (DTM). When the DSM is correctly normalized, structural forest parameters such as tree height, coverage percentage, timber volume or biomass can be accurately estimated. Tree height is obtained directly from the CHM, whereas coverage percentage can be obtained by image classification of canopy versus ground areas and measuring relative area occupied by the former.

When there is no preexisting DTM, it is necessary to realize a ground segmentation, by classifying reconstructed 3D points as belonging to ground or to the canopy. For this purpose, techniques typically employed for LiDAR point clouds can be used [18]. ODM performs this segmentation as part of its 3D cloud generation process using the Simple Morphological Filter (SMRF) [19]. On the other hand, Agisoft PhotoScan uses a progressive densification filter algorithm based on triangulation of lowest points. However, since both approaches assume that there are detectable ground points throughout the surveyed area (and this can not be granted when employing photogrammetry), canopy points are commonly misclassified as ground points. This drawback limits their use in forest environments.

In [7], a review of the state of-the-art in aerial photogrammetry in forest applications is presented. Authors conclude that it presents a highly accessible and versatile solution to the acquisition of very high-resolution 3D data and mention four of the main challenges for forest applications: *i) Reproducibility*, *ii) Availability of accurate Digital Terrain Models (DTMs)*, *iii) Lack of acquisition and processing protocols* and finally *iv) Image matching issues*. Reproducibility is challenging due to variation in illumination, atmospheric, and seasonal conditions, so does not guarantee the same results on different survey missions. This is also related to lack of acquisition and processing protocols,

[1] https://www.opendronemap.org
[2] https://www.agisoft.com

since these variations make it hard to find the best sensor and flight settings, currently undertaken based on the surveyor's experience. The generation of accurate DTM is crucial to obtain good results in structural forest parameters estimation. One challenge of low-cost UAS application is the need for a bare-earth surface. Photogrammetry has limitations related to cameras' poor capability of penetrating the tree canopy and the minimum number of images observing the same ground points, which is not always possible in dense forest environments. Because of this, some works propose to use highly accurate DTMs generated by ALS-based systems to normalize the photogrammetry data [20], but this makes the survey process longer and tedious. Recent lightweight LiDAR products have been available for UAS payloads. However, these products often have costs in the range of USD 50-100k, and are therefore too expensive for most operational UAS deployments [21]

Finally, the matching process results particularly challenging in forested areas due to the uniform texture of the canopy, self-repeating patterns and potential trees movements. This may cause incomplete or noisy 3D point clouds as a result. To overcome these issues, it has been suggested to increase the overlap between images and to use a higher flight altitude, since this increases the number of features per image and reduces distortions [22,23]. However, this approach either imposes the use of faster camera or slower flight speed (if the overlap is increased) or reduced effective resolution (due to higher flight altitude).

There are some works that study the impact of flight and camera settings on the 3D reconstruction quality. The relationship between overlap and the ground area represented by an image pixel, which is meant as Ground Sample Distance (GSD) is studied in [22]. Nevertheless, the generated point cloud density is used as a metric of quality without evaluating the cloud precision. Similarly, [24] analyze the influence of flight altitude, image overlap, and sensor resolution on forest reconstructions. The number of detectable features in several images or *tie points* is used as a metric for this analysis, resulting in an incomplete evaluation method since this is not really a guarantee for a high reconstruction quality. Moreover, in both works, the error in the reconstructed 3D point cloud is not measured and ground control points are not included.

Another key parameter affecting reconstruction is the camera angle. This factor is of particular importance when observing irregular 3D surfaces such as trees. In this line, [25] study reconstruction quality when the camera angle is at 45°, using a terrestrial laser to generate point clouds to compare results obtained from images. Authors also tested different flight patterns in order to improve reconstruction precision and successfully estimate some of the tree's radius. Nevertheless, authors mention that further work is needed to complete the study of relevant mission settings and their impact on the reconstruction.

A deeper study on the use of oblique images for 3D canopy reconstruction is presented in [26]. Authors also demonstrate an improvement in accuracy on crown cover estimation percentage and maximum canopy height. To analyze their results, authors built ground truth data from a terrestrial laser scanner. Similar work with oblique images in high-relief landscapes is addressed in [27]. There does not seem to be a consensus in the state-of-the-art regarding which camera angle produces the best result. In fact, from the various related articles, angles in the range from 10° to 60° are recommended [27].

In order to face the aforementioned challenges and perform controlled experimentation of flight and camera settings, an alternative is to use forest simulators. There are some examples of simulator based analysis of photogrametry in the literature. One such example is the *SyB3R* benchmark where a 3D synthetic scenario is generated [28]. This tool post-processes the captured images to make them more realistic, adding distortion and simulated camera noise. However, this simulator is not flexible and permits only predefined scenarios not including forestry. Another simulator that is widely used in

robotics is *Gazebo* [29], but this tool is designed to simulate the physics of a robot motion and is not really focused on realistic world scenarios, even less on forests.

The main contributions of this paper are:

1. The development of a highly realistic simulator based on Unity [30] video engine, which allows to generate synthetic forest images during a simulated UAS flight and perform controlled experimentation with repeatability guaranteed. Using this tool, a detailed and extensive evaluation of the impact of the flight and camera settings on forest 3D reconstruction is presented.
2. A novel method to generate accurate DTM in forest environments using only the UAS point cloud obtained from SfM reducing highly the cost compared with the LiDAR oriented approaches. In contrast to them, it considers the gaps typically found in image-based point clouds during points classification. Based on this method, the estimation of structural forest parameters and the automatic detection of selective logging are proposed.

.

2. Materials and Methods

2.1. Forest Simulator

We develop a high realistic forest simulator to enable controlled experimentation of realistic survey missions. It is based on the Unity graphics engine [30], which is a multi-platform framework and includes a terrain generation module based on a user-supplied height map, including ground textures and objects such as trees (either manually or randomly placed). Figure 1 shows the three different tree models included in Unity. Each tree can be customized by changing its size, color and orientation. Including custom tree models, modifying the scene lighting as well as setting camera parameters are also possible.

Figure 1. Three different types of tree used in the simulation, from left to right: palm trees, planifolia and conifers.

A series of image acquisition poses are generated to simulate a survey mission, following a predefined flight path, which involves setting the camera altitude and angle. The poses are generated using the desired frontal and lateral overlap parameters, just as during a real survey planning. For each position, a simulated camera is placed in the appropriate location and an image is acquired.

For the simulation of a GPS sensor, the center of the environment is geo-referenced by a given coordinate system (typically UTM). In this way, the pose of all acquired images will be in reference to the scene coordinate system. Finally, these poses are perturbed using random white noise. The simulator also supports ground control points, by manually placing markers on the ground as done in real-world survey missions.

After acquisition is complete, the simulator generates an image sequence where the GPS poses are recorded in the EXIF label. This allows the same reconstruction process to be followed that would be done for images acquired with a real camera on a real survey mission.

As ground-truth information the simulator also generates the terrain mesh (as a point cloud), the CHM and a segmentation of *ground* and *non-ground* points in this map (see Figure 2). The simulator can also be used to report the crown size and highest point of individual trees.

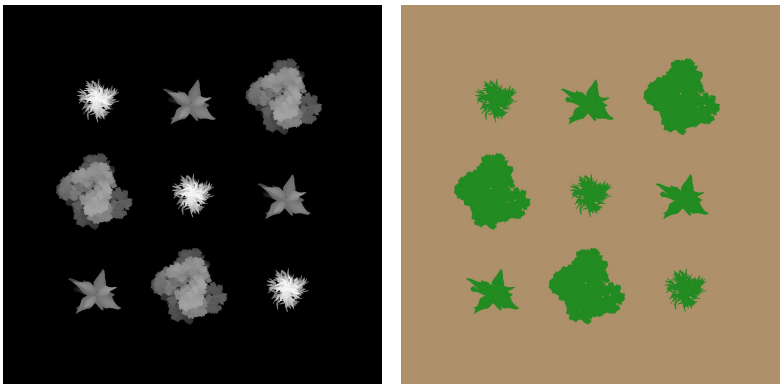

Figure 2. Exported information from the simulator. In the left is shown the height maps and in the right a segmentation of trees and floor for the 9Tree Scenario.

Two different scenarios were considered: *Simple Trees* (Figure 3 left) and *Yosemite* (Figure 3 right). The first scenario contains just nine trees of three different types spread over a square shaped region with flat terrain (see Figure 2). The second scenario aims to be a realistic representation of Yosemite National Park [31] by means of a real DTM obtained from LiDAR. Different tree types were randomly placed, followed by manual filling in some areas. Thus, the scenario results in a mix of both dense and sparsely forested areas.

Figure 3. Both synthetic scenarios used in this work: Simple Trees in the left and Yosemite in the right.

In this way, we are able to simulate survey missions with different settings over synthetic scenarios in which the position of each tree (and each leaf) is perfectly known.

2.2. Survey Mission Settings

We characterize two different types of survey mission settings regarding to: sensor and flight; and consider four metrics to evaluate the resulting reconstruction: flight time, image processing time, point cloud precision and ground-sample distance (GSD).

Since these variables are related in non-trivial ways, we present an analysis of these relations. Figure 4 outlines the relations between camera parameters and the rest of the survey settings and reconstruction metrics: arrows represent one parameter impacting in the value of another one, round nodes represent the four mentioned metrics.

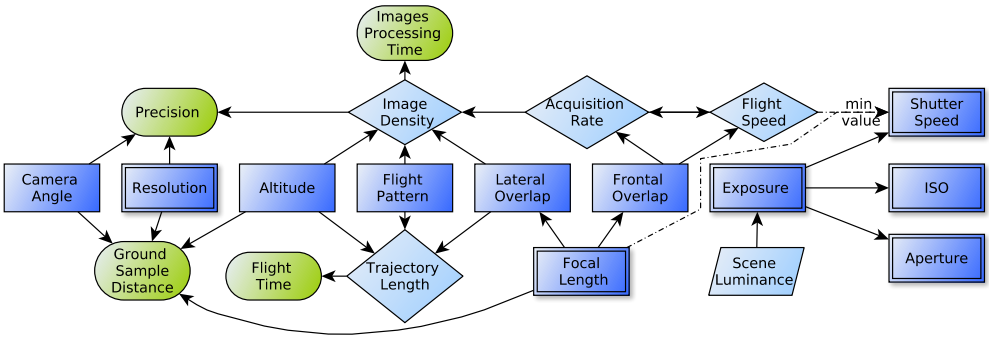

Figure 4. Square nodes denote user settable parameters (simple rectangles represent flight-related parameters while double border rectangles correspond to sensor related parameter), round nodes denote evaluation metrics, rhombuses denote *inferred* parameters and slanted rectangles denote non-controllable parameters. The continues line denotes that the node affects the final value, while the dash line represent a minor limit. These simplified scheme shows the most relevant relations between the settable (rectangles) and the control (rounded nodes) parameter that are relevant for these work.

We can further distinguish between user settings (those that must be explicitly chosen before the mission, represented with rectangles in the figure) and *inferred* settings (those indirectly affected by user settings, represented with rhombuses). Flight-related user settings are *image overlap* (%), *flight altitude* (m), *flight speed* (m/s), *flight pattern* (single or double grid) and *camera angle* (°). Sensor related settings are: *image resolution* (Mpx), *focal length* (mm), sensor sensitivity (ISO speed), *shutter speed* (ms) and *aperture* (f number). The inferred parameters in our model are: *image acquisition rate* (Hz), *image density* ($1/m^2$) and *trajectory length* (m). From these two groups is possible to estimate the value of the control parameters group (rounded green nodes): *precision* (m), *image processing time* (h), *ground sample distance* (cm/px) and *flight time* (s). These last group will be used to evaluate the reconstruction process. Finally, we can also identify some variables that are not under user control whatsover: *scene luminance* and *maximum acquisition rate*.

In general, there is no single configuration that guarantees a good reconstruction. To find the optimal parameter configuration, it is necessary to understand and quantify their effects. In the following sections we describe these variables and metrics in greater detail, discuss how they are related between each other and give some hints towards good starting points for configuring values.

To evaluate the impact of the survey mission settings described below we used the simulated scenario *Simple Trees* and processed the resulting images using ODM. For each configuration we repeated three times the cloud generation process and then we estimated the mean of three relevant parameters: 1) distance between centers of bounding box (BB) of the original and generated cloud; 2) points number and 3) BB size. We also used this parameters to detect wrong reconstruction when some thresholds are reach. In particular, if the BB was bigger than 100m in any direction, or the BB was 150% bigger or 50% smaller than expected, the reconstruction was rejected.

2.2.1. Overlap

One of the most important mission settings is the image *overlap*: the percentage of the image that intersects with other images taken nearby. The importance of this parameter lays in the fact that in order to create 3D geometry from images, at least two views of a portion of the surface are needed. Thus, the higher the image overlap, the greater chance of establishing correspondences. Furthermore, correspondences are used to set restrictions to the underlying SfM optimization and thus a large number of these usually results in increased reconstruction accuracy.

Image *overlap* is directly proportional to the number of *images per area*: to achieve high overlap, more images are needed over the same distance, resulting in a denser distribution. This also implies that the image *processing time* will be higher. In other words, this parameter is a direct trade-off between reconstruction precision and efficiency. We can further distinguish *frontal* (o_f) and *lateral overlap* (o_l):

$$o_f = (1 - \frac{d_f\, f}{H\, w})\, 100 \qquad (1) \qquad\qquad o_l = (1 - \frac{d_l\, f}{H\, w})\, 100 \qquad (2)$$

where d_f is the (longitudinal) distance between consecutive pictures (m), d_l is the (lateral) distance between flight lines (m) (see Figure 5), f is the focal length (mm), H is the distance from the camera sensor to the ground (m) and w is the sensor width (mm).

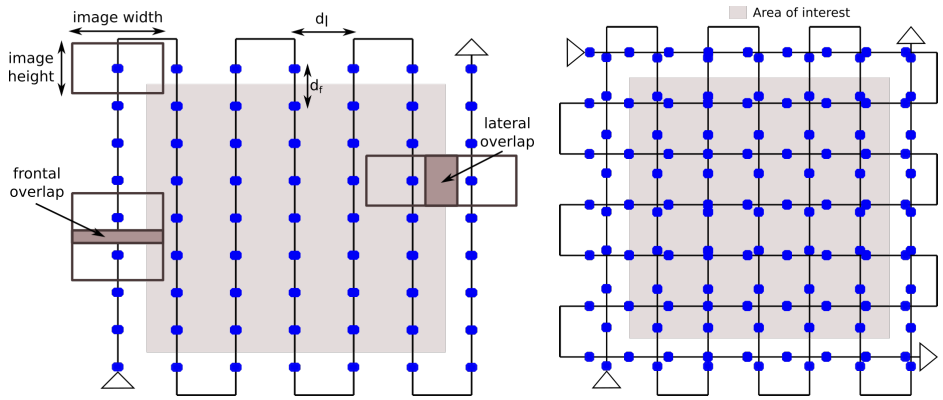

Figure 5. Two flight mission plans, in the left a simple grid and in the right a double grid plan. Blue dots represent the places were pictures are planned to be captured. Also frontal and lateral overlap are shown.

Frontal overlap depends on the image *acquisition rate*, since higher o_f implies that a greater number of images are acquired during the same time interval (assuming the flight speed remains constant). Thus, the combination of sensor capabilities and minimum flight speed will usually impose a higher bound on o_f. Increasing *lateral overlap* will reduce d_l. This means that a larger number of passes will be needed to achieve a tighter grid. The longer flight trajectory will result in higher *flight time* required (again, assuming constant flight speed). In conclusion, increasing o_l will bear the same benefits of larger o_f value but at the expense of longer survey missions, which will usually be limited by the flight autonomy of the UAS.

An alternative approach to increase o_f which does not impose a higher *acquisition rate* is to modify the *flight pattern* from a simple to a double grid (see Figure 5). This, of course, also negatively impacts *flight time*. For very irregular surfaces, such as the case of forest canopy, a high *image overlap* of at least 80% is usually recommended. As a rule of thumb, each point should be visible in at lease 4 to 5 images [7]. In this work, we tested values between 75% and 95% of both lateral and frontal overlap.

2.2.2. Flight Altitude

Flight altitude is also a trade-off between *flight time* and the reconstruction *precision*. If the image overlap is fixed, flying at a higher altitude will allow higher d_f and d_l. In other words, images will be taken further apart in time and space. Furthermore, as d_l is increased, the flight trajectory will be shorter (less passes are needed) and flight time will be reduced. However, this all comes at the expense of reduced GSD (each pixel will represent a larger ground area) and point-cloud precision (image correspondences will be less accurately established).

Again, for the case of forestry applications, a relatively low altitude (relative to canopy) is recommended to maintain sufficient reconstruction detail. If this is not possible for the complete area, surveys performed at different flight altitudes may be combined in a single reconstruction. In this work, we evaluated different flight altitudes between 50m and 200m.

2.2.3. Flight Pattern

The *flight pattern* determines the path the UAV will follow. For forestry applications the most used ones are simple or double grid in a squared or rectangular area (see Figure 5). Simple grid is less time consuming but double grid is more accurate since it has more images and from different sides. Thus, depending on the application it will be adequate to use one or the other. When generation of 2D maps is the main interest, the surface is mostly flat or the area to be cover is extensive the simple grid is usually used. For 3D models or when the surface has height variations (buildings, rugged terrains like precipices) and the surface to be covered is small the double grid will give better results. In general in order to improve the 3D models generation the *flight pattern* include a combination of different *camera angles* (in general nadir and another value) and sometimes even different *flight altitudes*. In this work, we tested both single and double grid patterns combining with different altitudes and camera angles.

2.2.4. Camera Angle

Camera angle is the tilt angle of the camera with respect to the ground, for example a camera pointing down correspond to 90^o, while a camera pointing foward to 0^o. *Camera angle* is an important parameter in the mission setting as adding oblique images allows observing new parts of the environment, such as the side of trees, generating richer reconstructions. But if the angle is too low, it may be difficult to match the images, as the area shared between them could be reduced due to occlusion. Also, if the horizon is observed, it will give a wrong reconstruction or directly an error in the SfM process, as the system will try to include this faraway areas in the reconstruction. In this work, we tested four angle values between 60^o and 90^o, using both a simple and double grid flight pattern.

2.3. Ground Sample Distance

The *ground sample distance* (GSD) is related to the detail obtained during the reconstruction in terms of the area represented by each image pixel:

$$\text{GSD} = \frac{p}{f} H \cos(\theta)^{-1} \tag{3}$$

where p is the sensor pixel size and θ is the angle between the nadir direction and the sensor line-of-sight. The factor $\cos(\theta)^{-1}$ only has an effect when the camera direction is not nadir [32].

2.4. Reconstruction Error

To measure the reconstruction error we consider the point cloud detail when compared to a reference mesh. For simulated survey missions we use the ground-truth mesh as a reference and obtain different metrics to compare it with the one obtained from the

reconstruction. For real-world missions, this could also be performed if a ground laser scan were available, but this is not usually the case. For this reason, in real-world survey missions we manually placed ground-control points from which we can later obtain a similar reconstruction error by computing the corresponding root-mean squared error (RMSE) between their known and reconstructed locations:

$$\mathrm{RMSE}(P_1, P_2) = \sqrt{\frac{1}{P} \sum_{p_1 \in P_1, p_2 \in P_2} \|p_1 - p_2\|^2} \tag{4}$$

where P_1, P_2 are the two sets of corresponding real and estimated coordinates of GCPs, and $P = |P_1| = |P_2|$.

2.4.1. Point Cloud Comparison

To evaluate the precision of a given simulated reconstruction we compare it with the one exported from the simulator using METRO [33]. This method estimates the distance between two surfaces, using one as pivot, by computing the euclidean distance of each point (of the other) and the closest point of the pivot. Given a point p and a mesh M the distance point-mesh is defined as:

$$e(p, M) = \min_{\tilde{p} \in M} d(p, \tilde{p}) \tag{5}$$

where d is the euclidean distance between two points. We can now define the root mean squared (RMSE) error between two meshes M_1 and M_2 as:

$$\mathrm{RMSE}(M_1, M_2) = \sqrt{\frac{1}{|M_1|} \sum_{p \in M_1} e(p, M_2)^2} \tag{6}$$

2.5. Digital Terrain Model Generation

The DTM describing all ground points in the environment is a key input to estimate canopy height and other forest structural parameters. In this section we propose a novel method to generate accurate DTM using only the point cloud. First, we perform an initial classification based on the Simple Morphological Filter (implemented in the ODM tool) [19], which assigns each point to either *ground* or *non-ground* class. To improve on this initial result, we then compute the best-fitting plane for all *ground* points and then reclassify all points by considering their distance to the plane. Finally, to close gaps in the ground point cloud, we also estimate a plane for each gap and generate points uniformly over this surface. In Figure 6 we show the scheme corresponding to the workflow described above. The SMRF [19] algorithm used by ODM to classified the cloud points utilize four parameters: *slope* (slope rise over run), *window* (max windows size), elevation *threshold* and *scalar* (elevation constants used to classified the cloud points as ground or not ground). ODM by default uses parameter settings which are not ideally suitable for forest reconstructions. In [19], an optimized parameter set is proposed for an area with low altitude and dense vegetation. Thus, for these experiments we tried both the default and optimized parameters, as well as up to eighty random combinations. To evaluate the results, we compared the final ground map to that the ground truth, obtained from the simulator.

The DTM is then constructed with the PDAL Library [34] using as input all *ground* points. After this, the CHM can finally be obtained by subtracting the height of the ground at each location to the z coordinate of every *non-ground* point in the DSM. The DSM is calculated similarly to the DTM, but using all the cloud points.

In the following sections, we describe the point-cloud re-classification and gap closing in more detail because they are the key steps of the method to obtain accurate DTM.

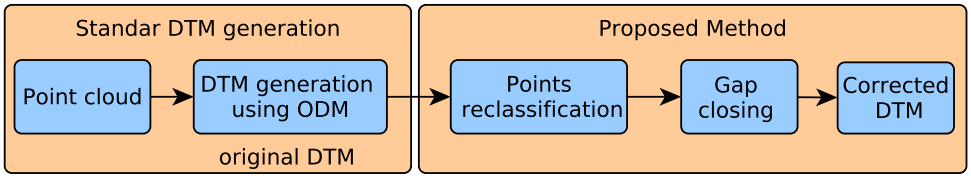

Figure 6. Workflow scheme for the digital terrain model generation using the proposed method.

2.5.1. Points Reclassification

From the already classified ground cloud, we first partition the points using only their X and Y coordinates (see below). Then, for each partition, we estimate the best-fitting plane using a RANSAC (Random sample consensus) scheme for robustness to outliers. Finally, we reclassify all points above the plane by some distance threshold as not *ground* and all points closer as *ground*. The pseudo-code for this step is presented in Algorithm 1.

Algorithm 1 Reclassification of Ground Points

```
1: procedure GroundReclassification(GroundCloud)
2:     partitions = Partition(GroundCloud)
3:     for i=1:#partitions do
4:         plane = RANSAC(partitions[i])
5:         for j=1:(#point ∈ partitions[i]) do
6:             if Height(point[j])>Height(plane)+threshold then
7:                 GroundCloud = GroundCloud - point[j]
```

To partition the cloud points, we considered four alternatives: *i) Plane*, which considers the entire cloud as a single partition and use only one plane to adjust it; *ii) Uniform Division*, an iterative method that divides the cloud in four uniform sections, and continues recursively until either the area covered by each subdivision or the number of points contained in it are below a given threshold; *iii) Median Division*, similar to the uniform division, but considering the median of the points number in each area instead. The main idea is to have partitions with the same points number and *iv) Surrounded*, which attempts to find good planes in the areas without points (generally corresponding to dense tree areas), using the border of them to estimate the best plane. The first step is to find all the areas without points, and create a partition for each one containing all the surrounded points. After this, all the remaining points of the cloud are assigned to the same partition.

2.5.2. Gap Closing

To fill all gaps remaining in the point cloud of *ground* points, we apply a gap closing algorithm. We follow a similar approach as for reclassification by closing each gap by means of a plane. From the ground points of the reclassified cloud, and using the surrounded method we separate the cloud in several partitions. Each gap has associated one partition, and using RANSAC we estimate the best plane for each one. After this, equidistant points are generated over the plane and added to the ground cloud. Algorithm 2 describes this step of the method.

2.6. Structural Parameter Estimation from SfM

In this work we focus on two main forest structural parameters than can be obtained using SfM techniques: tree coverage and height. While computing tree height can be generalized to obtaining the CHM, tree coverage can be estimated by the ratio of forested to total area:

Algorithm 2 Ground Extension

```
procedure GROUNDEXTENSION(GroundCloud)
    partitions = PARTITION(GroundCloud)
    for i=1:#partitions do
        plane = RANSAC(partition[i])
        points = CREATENEWPOINTS(plane)
        GroundCloud = GroundCloud + points
```

$$\text{coverage} = \frac{(\#\text{TreePixels})}{(\#\text{GroundPixels}) + (\#\text{TreePixels})} * 100 \tag{7}$$

where (#TreePixels) is obtained directly from regions of the CHM with non-zero height (considering a threshold). While the CHM could be used to obtain individual tree height, it is generally more useful to a height based segmentation of the CHM, considering that forested areas usually shows sectors with markedly distinct height (due to different successional stage, dominant species, soil condition or management).

2.7. Selective Logging Detection

Selective logging detection results from comparing reconstruction of the same surveyed area at different times. First, the CHM corresponding to each survey is computed as explained in previous sections. The ground-referenced point clouds are then aligned and the difference is computed, using the oldest as a reference. Algorithm 3 describes the procedure.

Algorithm 3 Changes Detection

```
procedure CHANGESDETECTION(Cloud_a, Cloud_b)
    (cgeCloud_a,cgeCloud_b) = CORRECTGROUNDEST(Cloud_a, Cloud_b)
    (alCgeCloud_a) = ALIGNCLOUDS(cgeCloud_a,cgeCloud_b)
    (CHM_1,CHM_2) = CHM(alCgeCloud_a,cgeCloud_b)
    diffMap = DIFF(CHM_1,CHM_2)
    binDiff = BINCLASCHANGE(diffMap)
    binDiff = MORPHFILTER (binDiff)
    binDiffContourns = CONTOURS(binDiff)
    binDiffContourns = MINAREAFILTER(binDiffContourns)
```

The first step is to use the correction in the ground estimation described previously with the function CORRECTGROUNDEST for both clouds, to then align them using ALIGNCLOUDS. After this, both CHM maps are generated with the CHM function, to then calculate the difference between them. The function BINCLASCHANGE uses a threshold to classified every point as changed or not. This threshold is defined as a third of the altitude of the highest point since this value exceeds the noise and at the same time detects changes in the trees; however, the user can change it manually. The function MORPHFILTER applies two morphological filters (first erotion and then dilatation) in order to eliminate noise, and the same filters in the inverse order, to eliminate little holds in the big forested areas. Finally, the contours are calculated with CONTOURS and then a minimal area filter is used to eliminate small areas with MINAREAFILTER.

2.8. Fieldwork

Finally, we performed a series of real-world experiments both for the ground segmentation step and structural parameters estimation. These experiments where carried out in forested environments located in different protected areas in Argentina and using different UAVs. In Nahuel Huapi National Park (Neuquén Province) where surveyed an area of 200 x 200 meters using an DJI Mavic 2 Pro UAV. In Ciudad Universitaria-

Costanera Norte Ecological Reserve in Buenos Aires City, we used a DJI Phantom III Standard to made a 3D model in an area of around 20 hectares. In Ciervo de los Pantanos National Park (Buenos Aires Province) we used a custom built fixed-wing aerial platform based on the commercial Skywalker 1900 fuselage.

3. Results and discussion

The first set of experiments are focused on establishing certain aspects regarding the survey mission setup with simulator 3.1. The second set of experiments are aimed towards experimental validation of the DTM generation method 3.2. Third, forest structural parameters estimation is presented 3.3. Finally, selective logging detection process using the proposed DTM generation method is also validated 3.4.

3.1. Survey Mission Settings Analysis

In this section we evaluate the impact of some of the main survey mission settings over the SfM reconstruction process. For this experiment we use the simulated scenario *Simple Trees* and processed the resulting images using ODM.

3.1.1. Overlap

As previously mentioned, image overlap is strongly related to reconstruction quality since it mostly determines the number of correspondences that can be established between adjacent images (the higher the overlap, the higher the matches). We initially tested values between 75% and 95% of both lateral and frontal overlap to determine a usable range of values. We then focused on overlap values in the range between between 85% and 95%, considering also that values are usually recommended for SfM reconstruction of forests. Results of these experiments are presented in Table 1.

Param	N Img	N Points	FD(m)	RMSE (m)
F 75% L 75%	12	0.6M	378.12	8.32
F 85% L 85%	24	1.2M	466.70	4.37
F 85% L 88%	30	1.5M	569.12	3.58
F 85% L 92%	48	2.4M	874.64	4.10
F 85% L 95%	72	3.7M	1261.83	2.62
F 88% L 85%	28	1.4M	451.15	2.19
F 88% L 88%	35	1.8M	549.67	2.30
F 88% L 92%	56	2.9M	843.52	2.59
F 88% L 95%	84	3.6M	1215.16	2.47
F 92% L 85%	40	1.5M	451.15	2.02
F 92% L 88%	50	1.9M	549.67	1.85
F 92% L 92%	80	2.9M	843.52	1.68
F 92% L 95%	120	4.1M	1215.16	1.61
F 95% L 85%	64	3.3M	466.70	1.29
F 95% L 88%	80	3.7M	569.12	1.95
F 95% L 92%	128	5.8M	874.64	1.77
F 95% L 95%	192	9.4M	1261.83	1.32

Table 1: Quality metrics for different overlaps: **N Img** (number of images), **N Points** (number of points), **FD** (flight distance) and **RMSE** (Root Square Mean Error). In blue, is shown the best five results for each metric, and in dark gray a good option for the trade-off between precision and overlap is remark.

When analyzing the results of these experiments we can see a direct relation between image overlap and the number of images and, thus, the number of generated 3D points. Moreover, lateral overlap has greater impact over these variables since it results in a tighter flight path with more passes over the survey area. As expected, values lower than 85% do not give usable results.

We can also analyze the effect of varying either frontal or lateral overlap leaving the other parameter fixed (see Figure 7). We can see that when lateral overlap is increased and frontal overlap is left fixed, flight distance increases as previously mentioned. Conversely, when frontal overlap is increased and lateral overlap is left fixed, flight distance remains mostly constant. Finally, we can observe that precision mostly increases depending on frontal overlap, whereas increasing lateral overlap doesn't have a big impact of precision.

From all of these combinations we found that using 85% lateral overlap gives good results overall. In particular, combining this value with 95% overlap gives the best trade off in terms of accuracy and number of points/images and flight distance. These results are in line with previous analysis, in particular with those obtained in [24], where the authors also analyzed separately the effects of both forward and lateral overlap, although using a video footage.

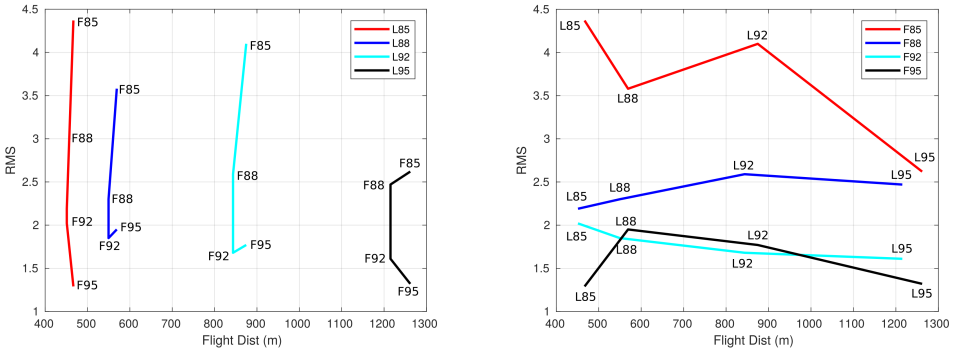

(a) Lateral overlap variation. (b) Frontal overlap variation.

Figure 7. Flight distance versus the RMSE error, for different values of frontal and lateral overlap

3.1.2. Camera Angle and Flight Pattern

In this experiment we analyzed the effect of different camera angles on the reconstruction. We tested four angle values between 60° and 90°, using both a simple (see Table 2) and double grid (see Table 3), using a flight altitude of 100m with a frontal and lateral overlap of 95% and 85%, respectively. We did not consider angles lower than 60° since in general too much sky would be visible in the pictures and this brings problems for the image processing pipeline.

When comparing single grid flights with different camera angles, the first thing to note is the increment of points in the clouds for bigger angles. This can be attributed to the fact that although for small angles the observed surface is grater, the overlap between images is reduced. Nevertheless, regarding reconstruction precision, we do not find significant differences when the camera angle change.

Angle	N Img	N Points	RMSE (m)
$\alpha = 60^o$	64	2.1M	1.91
$\alpha = 70^o$	64	2.7M	1.90
$\alpha = 80^o$	64	3.1M	1.97
$\alpha = 90^o$	64	3.3M	1.51

Table 2: Quality metrics for different camera angles. Blue values represent the best result.

For the double grid case (see Table 3) we repeated the experiment, considering that now the angle may change between either orientation of flight lines (thus we will name each angle α_1 and α_2). In general we can see a similar behavior than for a simple grid: higher angles lead to higher precision and more 3D points. Regarding recontruction

presition, for both overlap cases, the configuration $\alpha_1 = 90^o$ and $\alpha_2 = 60^o$ show the best results, especially for the lower image overlap case, where the number of 3D point is smaller. This result reinforce that obtained by [26,27], showing the relevance of incorporate oblique images to make 3D reconstructions in forest landscapes.

Angles	N Img	N Points	RMSE (m)
DG F95% L85%			
$a_1 = 60^o \wedge a_2 = 60^o$	128	4.4M	1.75
$a_1 = 70^o \wedge a_2 = 70^o$	128	5.6M	1.45
$a_1 = 80^o \wedge a_2 = 80^o$	128	6.3M	1.83
$a_1 = 90^o \wedge a_2 = 60^o$	128	5.6M	0.91
$a_1 = 90^o \wedge a_2 = 70^o$	128	6.2M	0.99
$a_1 = 90^o \wedge a_2 = 80^o$	128	6.6M	0.93
$a_1 = 90^o \wedge a_2 = 90^o$	128	6.7M	0.94
DG F90% L80%			
$a_1 = 60^o \wedge a_2 = 60^o$	48	1.7M	2.1
$a_1 = 70^o \wedge a_2 = 70^o$	48	2.1M	2.67
$a_1 = 80^o \wedge a_2 = 80^o$	48	2.4M	2.57
$a_1 = 90^o \wedge a_2 = 60^o$	48	2.1M	1.27
$a_1 = 90^o \wedge a_2 = 70^o$	48	2.3M	2.32
$a_1 = 90^o \wedge a_2 = 80^o$	48	2.3M	2.58
$a_1 = 90^o \wedge a_2 = 90^o$	48	2.5M	2.63

Table 3: Quality metrics for different camera angles in a double grid setup. Blue values represent the best result for each configuration.

3.1.3. Flight Altitude

For the single grid case (Table 4), as expected higher altitudes result in a smaller number of images and 3D points. This in turn shorten flight distance but also reduces precision.

For the double grid case, we tested combinations of different altitudes for flight lines in each orientation (Table 5). In this case, while there's also a decrease in the number of images, 3D points and flight distance as altitude increases, we can see that precision not always decrease, in particular the configuration corresponding to the best precision for this experiment was $h_1 = 50$m and $h_2 = 150$m.

3.2. DTM generation and ground segmentation

We performed a series of experiments to evaluate our DTM generation method and the ground segmentation required to ultimately obtain a CHM. To establish a baseline, we first perform a segmentation using ODM over the ground-truth point-cloud obtained from the simulator. We then attempt to improve this result by considering the different segmentation strategies.

Param	N Img	N Points	FD(m)	RMSE (m)
$h_1 = 50$	96	3.3M	669.81	2.13
$h_1 = 100$	24	1.2M	341.39	2.20
$h_1 = 150$	12	0.3M	246.32	3.07

Table 4: Quality metrics for different altitudes for simple and double grid options (FD: flight distance) with a frontal and lateral overlap of 90% and 80%, respectively.

Param	N Img	N Points	FD(m)	RMSE (m)
$h_1 = 50 \wedge h_2 = 50$	192	18.5M	1440.53	1.79
$h_1 = 50 \wedge h_2 = 100$	121	5.8M	1123.82	1.98
$h_1 = 50 \wedge h_2 = 150$	109	5.4M	1058.19	1.42
$h_1 = 50 \wedge h_2 = 200$	105	5.3M	1075.30	2.02
$h_1 = 100 \wedge h_2 = 100$	49	2.2M	714.99	2.14
$h_1 = 100 \wedge h_2 = 150$	37	1.5M	647.18	2.20
$h_1 = 100 \wedge h_2 = 200$	33	1.3M	671.16	2.00
$h_1 = 150 \wedge h_2 = 150$	25	0.5M	603.62	2.73
$h_1 = 150 \wedge h_2 = 200$	21	0.4M	592.75	2.66

Table 5: Quality metrics for different altitudes for simple and double grid options (FD: flight distance) with a frontal and lateral overlap of 90% and 80%, respectively.

Ranking	Slope	Win	Th	Scalar	Mean	RMSE
Best	0.18	17	0.5	1.5	1.257	2.653
Default	0.15	18	0.5	1.25	1.328	2.705
Optimized	0.05	11	0.15	2.3	1.648	2.965

Table 6: RMSE error for different settings of the ODM Ground Segmentation. The Optimized corresponds to the values recommended in [19]. **Win** stand for Windows and **Th** for Threshold.

3.2.1. ODM classification

In first instance, we compared different parameters settings in the ODM algorithm. Table 6 shows the results of default, optimized [19] and the best option among the eighty random combinations evaluated.

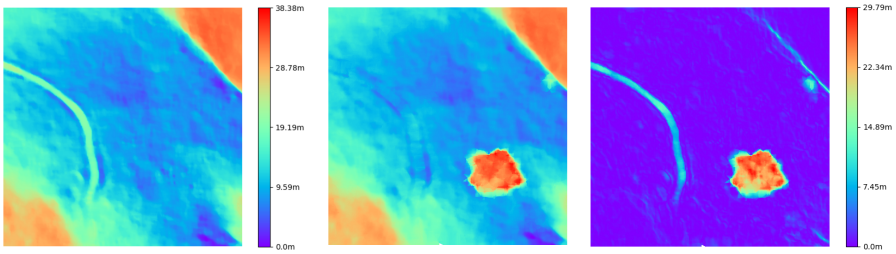

(a) Ground-truth DTM. (b) Estimated DTM. (c) Difference.

Figure 8. In the left and the middle are shown the DTM ground truth and the one obtained with the best set of parameters of Table 6, respectively. In the right, the error (calculated as the difference between the other two maps) in the DTM estimation.

In Figure 8 we also compare the ground-truth DTM to the one obtained by the aforementioned ground classification method (with the best set of parameters). When observing the difference (Figure 8(c)) between ground-truth (Figure 8(a)) and estimated (Figure 8(b)) we can identify three areas with large errors, which correspond to an open ditch on the left, a large group of trees in the middle and a small slope and a tree in the top right part.

3.2.2. Point Reclassification

In this section we evaluate the improvement of our point reclassification method over the initial result obtained directly from ODM. We tested the four cloud segmentation strategies, described in section 2.5.1. In Figure 9 we show the partitions generated as a

result of applying each strategy. The reclassification process is then performed in each partition and the final DTM is generated.

The Median method present the best results since it eliminates the wrong classified area corresponding to the dense trees, without affecting the rest of the scenario. Nevertheless, none of the methods show improvement related with the other two areas of error (the open ditch on the left and the slope on the right). The method of one plane also removed these point, but since only one plane was used and the terrain was not flat, the corners were wrongly classified as not ground, because the difference with the plane was too big. Something similar happened with surrounded method, since also use one plane for all the terrain. Finally, the uniform method was not able to remove the point of the dense tree area, since this area was too large and different partitions were set, making it impossible to estimate a good plane.

From each DTM we measure the error as in the previous section (figure 10). White areas corresponds to extend zones that were reclassified as not ground, and the interpolation of ODM can not fulfill those areas. It is desired to have them in wrong classified areas in the original DTM, but not in well classified zones. This areas will be fulfill again in the ground extension process.

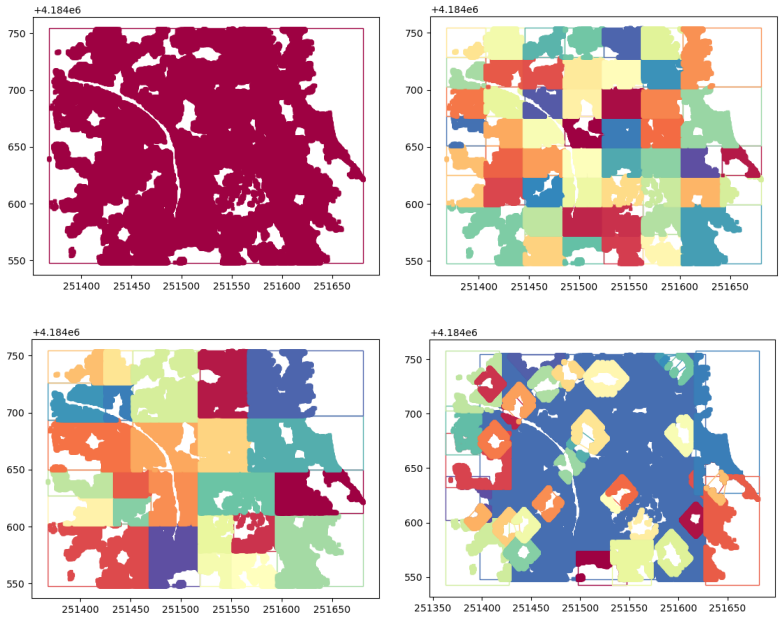

Figure 9. Partition used in ground points reclassification: top left *One Plane*, top right *Uniform*, bottom left *Median* and bottom right *Surrounding*.

Method	Mean Error	RMSE	Max Error	Cov %
One Plane	1.289	3.292	20.755	87.51
Uniform	1.273	3.803	29.670	99.83
Median	0.746	1.701	17.454	98.79
Surrounded	0.986	2.629	23.345	97.67

Table 7: Comparison, using *METRO*, between the different partitioning methods and the original mesh. **Cov %** is the coverage percentage of the original model. The *Median* method shows the better performance in all the metrics.

Using Metro we compared these DTM estimation with the ground truth, and the results are shown in Table 7. Again, Median partitioning method has the best performance.

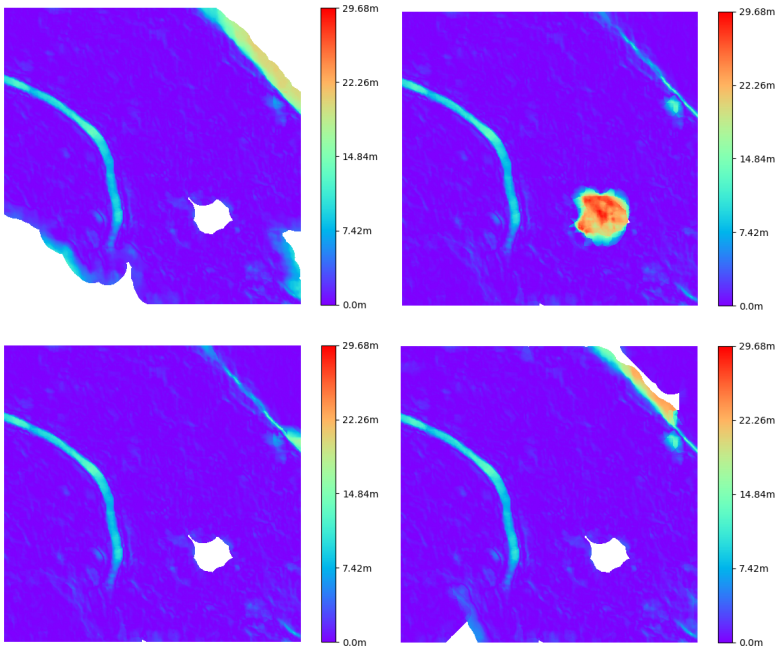

Figure 10. DTMs errors after reclassified as not ground some points (white areas) using the proposed methods: top left *One Plane*, top right *Uniform*, bottom left *Median* and bottom right *Surrounding*..

3.2.3. Ground Extension

For each of the reclassification results obtained in previous section, we then apply the ground extension method proposed in 2.5.2. As an example, in Figure 11 we show how points are added in gaps for one of these cases.

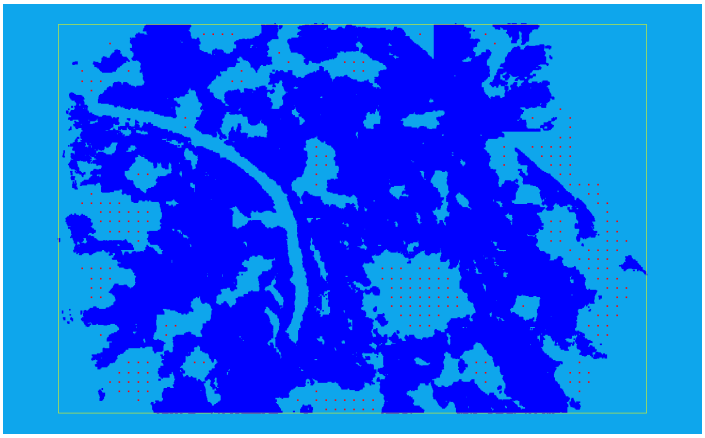

Figure 11. Added points (red) in the cloud for a distance of 5m.

In Table 8 we show the new results after applying the ground extension step. Observing these results, we realize that the *Surrounded* method shows the best performance.

Finally, in Figure 12 we compare the final DTM obtained via ODM and the improved one after applying the reclassification and ground extension methods with the *surrounded* strategy. We can here see that our approach considerably improves the result, which corresponds to an RMSE improvement from 4.287 to 1.843.

3.2.4. DTM in real-world cases

For the study area in Nahuel Huapi National Park, the resulting orthomosaic is presented in Figure 13(a) and the DTM obtained via ODM with the default configuration

Method	Mean Error	RMSE	Max Error	Cov %
One Plane	0.921	2.074	26.885	100
Uniform	0.828	1.868	21.661	100
Median	0.812	1.865	23.694	100
Surrounded	0.789	1.843	29.159	100
ODM	1.458	4.287	30.012	99.84

Table 8: Comparison, using *METRO*, between the different partitioning methods and the original mesh. The *Surrounded* method shows the better performance in all the metrics, and shows a bigger improvement in comparison with the default method used by ODM.

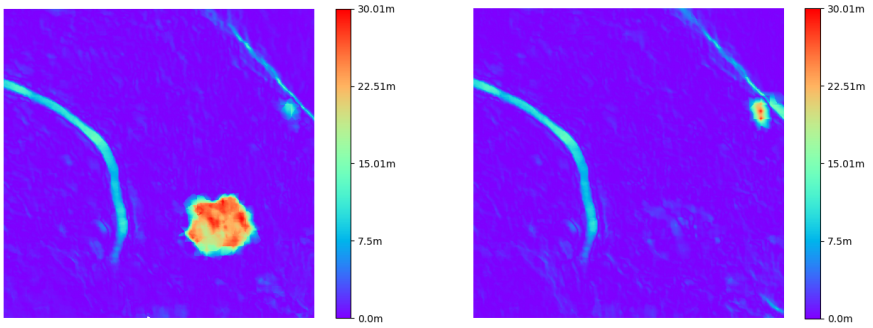

Figure 12. Differences within the original method used for ODM (left), and out proposed method (right) to estimate the ground.

is presented in Figure 13(b). We can observe that on the right of the image there are some trees (red areas) that were classified as ground and that there are also gaps (white areas) in the map. These issues occur since most of the surface is covered by trees and the default classification method is unable to correctly detect the ground. Both of these problems are solved when using the Algorithm 2 (see Figure 13(c)), were a mostly flat terrain is detected.

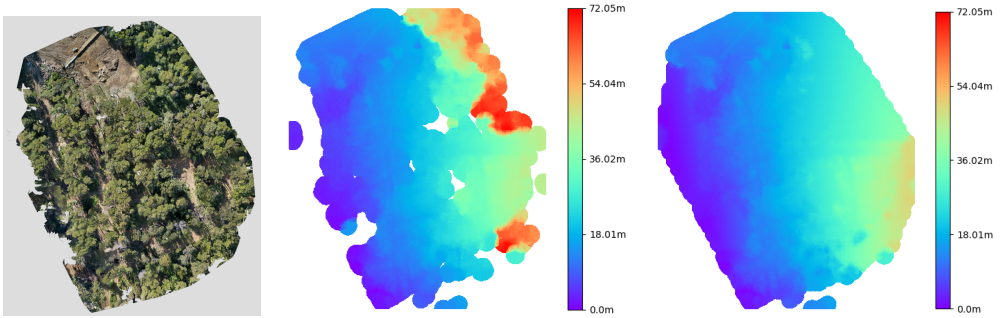

(a) Orthomosaic. (b) Default. (c) Proposed Method.

Figure 13. Original orthomosaic of the relevated area (left), DTM with the *Default* algorithm of ODM (middle) and DTM corrected with our method.

Figure 14 shows the results obtained for Ciudad Universitaria-Costanera Norte Ecological Reserve. Orthomosaic is in the left side, where is possible to observe this area. The middle image correspond to the default DTM, where again some of the trees are wrongly classified as ground and also there are some gaps. When running Algorithm 2 (right) with the same parameters as in the other reconstructions, the gaps are well estimated and disappear. Nevertheless, some areas are wrongly fulfill assuming a flat terrain, during the ground extension. This can be easily corrected by delimiting the border of the reconstruction.

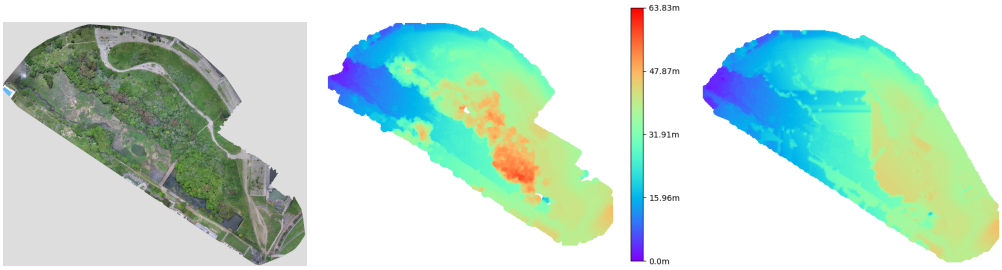

Figure 14. Original orthomosaic of the relevated area (left), DTM estimated with the *Default* algorithm of ODM (middle) and DTM corrected with our method.

3.3. Structural Parameters

In this section we present our results when estimating the structural parameters of interest: tree coverage and canopy height.

3.3.1. Coverage

Once ground segmentation is performed, estimating tree coverage is trivial since it reduces to computing the percentage of pixels classified as ground with respect to the total area in question. We can use the Yosemite simulated scenario again to compare tree coverage results to ground-truth information. When using ODM, the resulting coverage is 36.56%. With our approach coverage is 40.86%. Compared to the ground-truth value of 46.80% we can indeed observe our method results in an improvement. This measurement shows the importance of precise ground segmentation as it directly impacts coverage computation. Figure 15 shows the tree segmentations obtained for each method and the difference to ground truth segmentation.

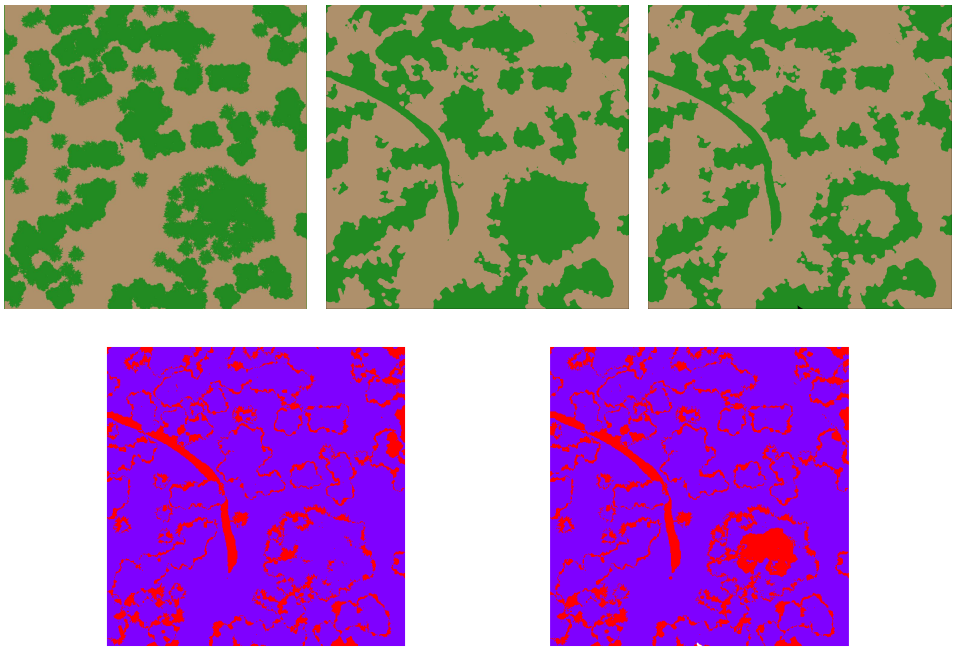

Figure 15. Top left: Expected segmentation from the real mesh. Top middle: segmentation using the ground estimation correction. Top right: segmentation with the default ground estimation. Bottom: difference between the expected segmentation and, at left, the one with the ground estimation correction and at right, with the default estimation.

On the other hand, we also compute tree coverage for real-world experiments. Since in this case we do not have ground-truth information only qualitative analysis is

performed. In Figure 16 we overlay the segmentation result over the orthomosaics of *Villa La Angostura* and *RECN* experiments. In general we can observe that most of the forested areas are correctly classified as not ground. The coverage percentage for *Villa La Angostura* is estimated as 45.53% and 17.60% for *RECN*.

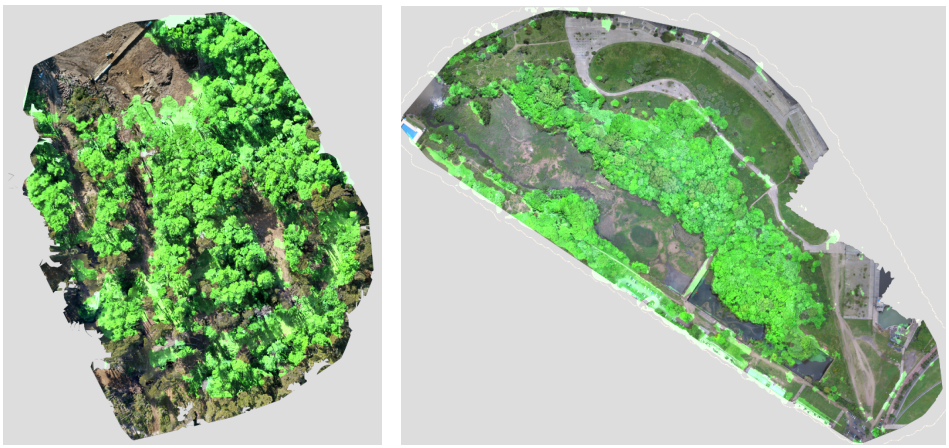

(a) VLA. (b) RECN.

Figure 16. Overlay between orthomosaci and the areas covered by trees (fluor green) for the *Villa La Angostura* and *RECN* experiments.

3.3.2. Tree Height

A second result we can obtain from the CHM is tree height. As previously mentioned, as detecting individual trees is not really feasible for very densily forested areas, we can resort to obtain a height segmentation from the CHM for the purpose of isolating potentially different forest types.

In Figure 17 we show the regions with similar tree height for a reconstruction of the *Ciervo de los Pantanos* national park in Buenos Aires, Argentina. To build this segmentation map we extended ODM software to allow specifying different height intervals to be mapped to a class (based on knowledge of available forest types in the area).

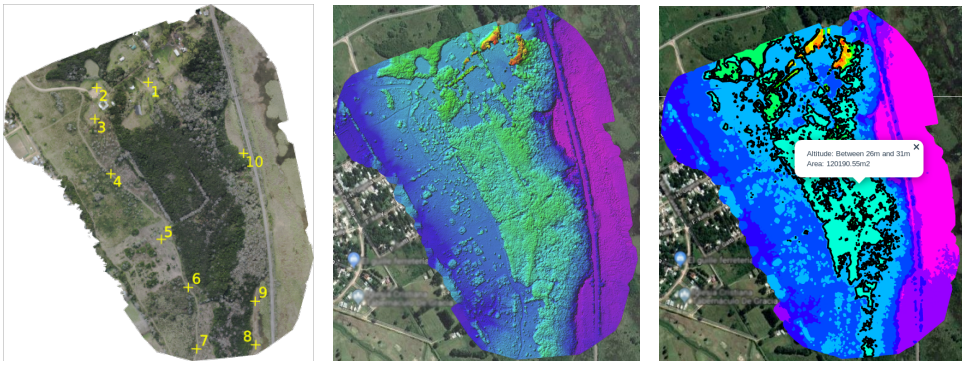

Figure 17. National Park Ciervo de los Pantanos. Left: Orthomosaic generated, where yellow marks represents the CGPs. Medium: corresponding height map. Right: segmentation stratified by heights.

3.4. Selective Logging Detection

In this section we evaluate the ability of our system to detect changes between two survey missions of the same area at different times. In the context of forestry, this feature has multiple applications such as selective logging detection. We performed two sets of

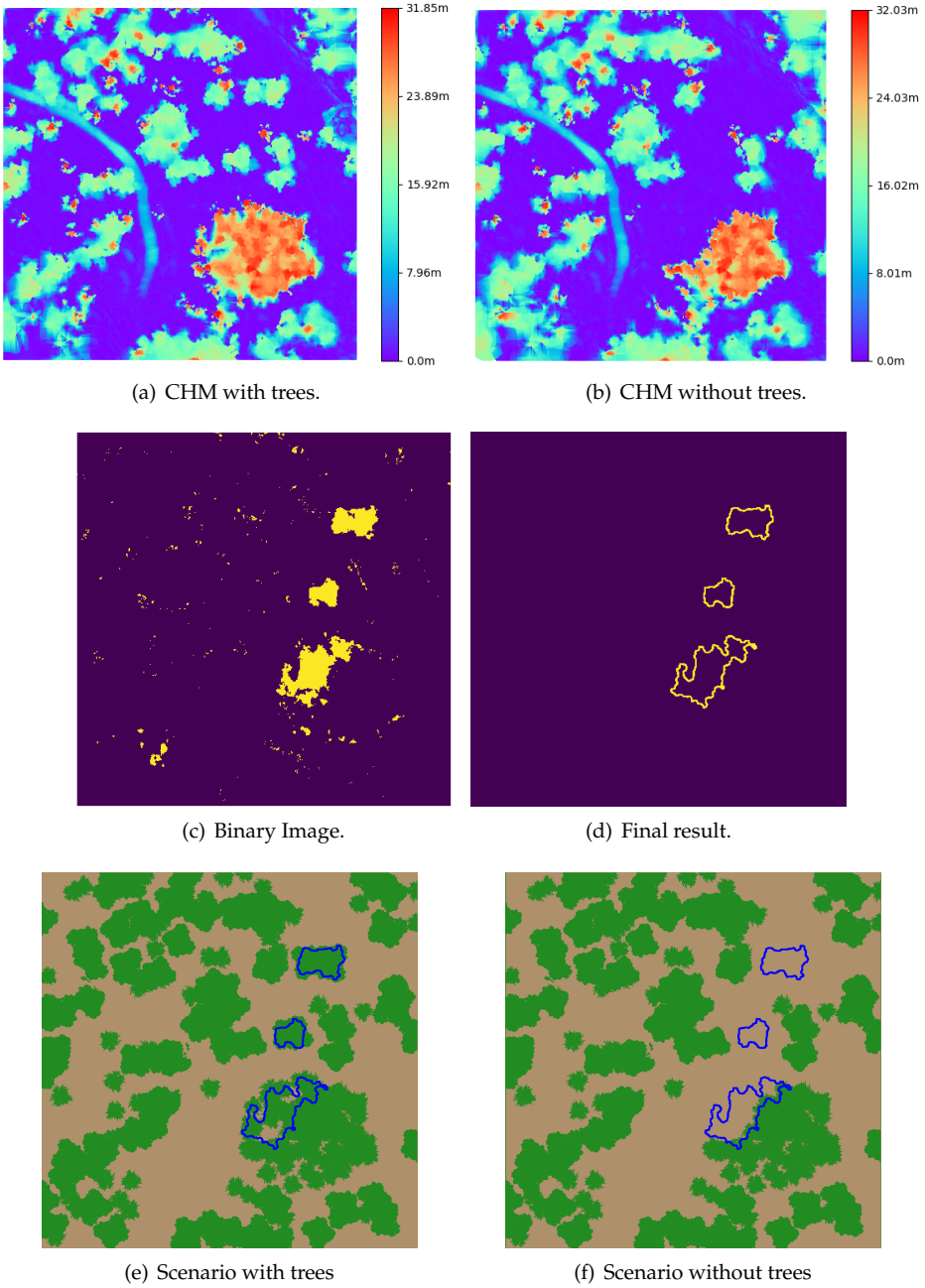

(a) CHM with trees. (b) CHM without trees.

(c) Binary Image. (d) Final result.

(e) Scenario with trees (f) Scenario without trees

Figure 18. Change detection process for *Yosemite*.

experiments: first in the *Yosemite* simulated environment and then on real-world scenario of a construction site inside a forested area.

3.4.1. Simulation

In this experiment we generated an initial tree population in the *Yosemite* simulated environment and then a second one with some of these trees removed from three different areas of the map. We performed two simulated survey missions and then attempted to detect the differences.

Figure 18 shows the change detection process step by step: Figure 18(a) and 18(b) show the resulting CHM for each mission. This cover a variety of different situations common on forests. The difference between both CHMs is computed and a binary map is generated (see Figure 18(c))) based on a user-defined threshold. Finally, a morphological

filter and contours are computed (selecting only those of a given minimum size), which gives the final result of detected changes (see Figure 18(d)). In this case we can observe that the three groups of removed trees are correctly detected. This can be confirmed by overlapping these contours over the scenarios with and without trees (see Figure 18(e) and Figure 18(f)).

3.4.2. Real Word Experiments

To study the performance of our selective logging detection method in real-world conditions a second set of experiments were performed on an area where selective logging was authorized. Due to the size of the area and safety constraints within the construction site, these experiments were carried out with the *DJI Mavic 2 Pro* commercial multi-rotor.

Three flights were performed at different times over two separate areas (of approximately 150x200 meters each) in Nahuel Huapi National Park, near Villa La Angostura. Due to technical difficulties it was not possible to use GCPs for all the flights. This issue had the effect of higher drift in the absolute position of the clouds. Nevertheless, since we perform point cloud alignment this issue is easily overcome. Of course, for larger areas, GCPs would be necessary to avoid warping of the point cloud.

For the first area (Figure 20(a) to 20(c)), after the initial flight, three trees of approximately 30m in height were cut down and, for before the final flight a quite larger area of trees was removed. The changes detected in the canopy structure after the second and third flight were correctly identified (marked in blue), as seen in Figures 20(b) and 20(c).

For the second experiment (Figures 20(d) to 20(f)), the section of trees removed is smaller and thus allows to see the performance on a more challenging case. In Figures 20(e) and 20(f) we show the detection results which again reflects the areas where selective logging was performed. This example also demonstrates that recognizing these changes could be quite difficult for a human, but an automated approach can be successful.

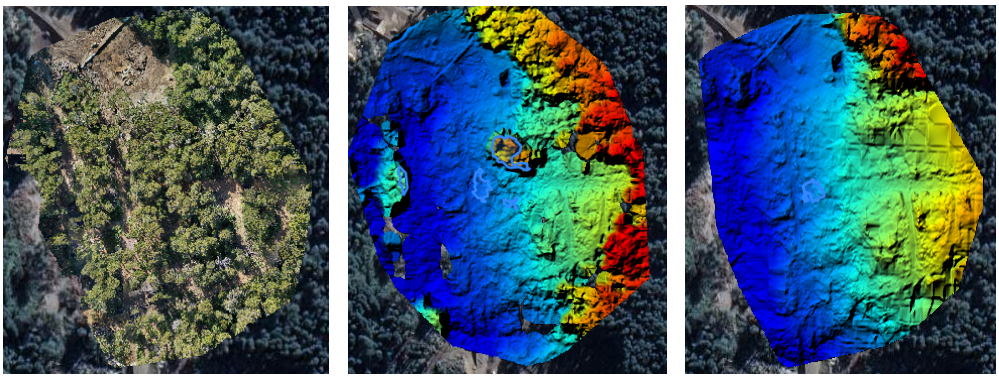

(a) Orthomosaic. (b) Original DTM. (c) Corrected DTM.

Figure 19. COMPLETE THIS

4. Conclusions

In this work we approached the problem of forest structural parameters estimation using aerial photogrammetry. We analyzed two relevant issues: the selection of survey mission and sensor settings and the generation of DTM using camera sensor in forests. For the first one an exhaustive analysis is presented using a custom-built highly realistic simulator that allows experimental repeatability. For the second issue we propose a new method to generate the DTM in forested environments using only the point cloud from SfM. Finally, we tested our method in real-world cases using different UAVs in natural forest areas.

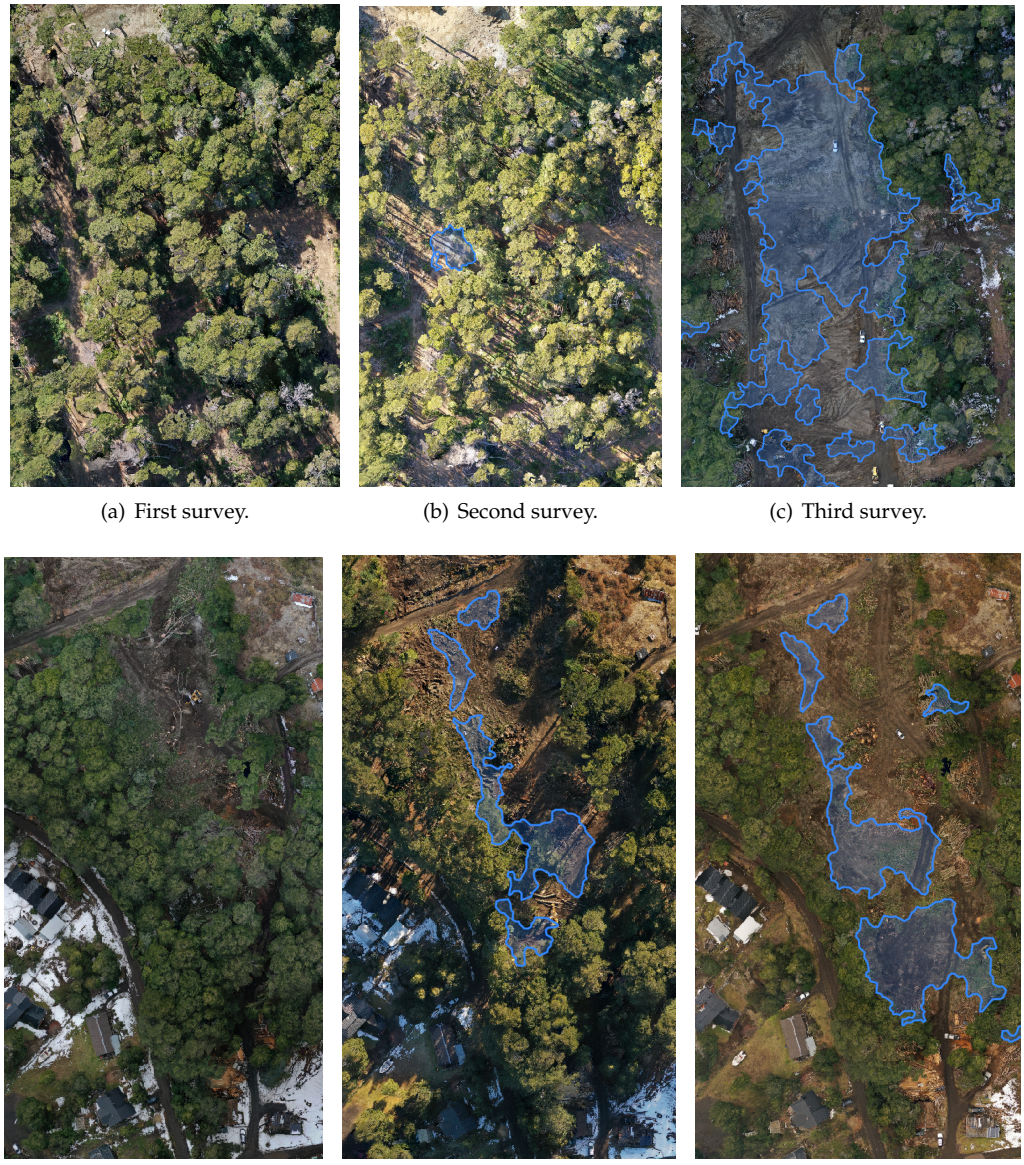

(a) First survey. (b) Second survey. (c) Third survey.

(d) First survey. (e) Second survey. (f) Third survey.

Figure 20. Orthomosaics obtained from two flights (first flight, top row, second flight, bottom row). Leftmost image is the reference orthomosaic and middle and rightmost ones are from the two following flights over the same areas, after different trees were cut down. Areas detected by our detection system are highlighted in blue.

In first place we studied the impact of flight settings in the final 3D reconstruction quality. We tested different configurations of image overlap, camera angle, flight pattern and altitude. The use of a simulator allowed us to realized hundreds of experiments and to count with a ground-truth to compare the obtained results. For the overlap we found that it is beneficial to use the highest possible value of frontal overlap, taking into account hardware capabilities (image rate) and the required processing time. Moreover a lower value of lateral overlap is also preferred as it results in lower number of images but with similar precision in the reconstruction. Frontal and lateral overlap of 95% and 85% respectively have shown to give the best results for forests. For the camera angle in single grid configuration a nadir angle shows better results than when using smaller angles, as the number of points is increased while RMSE is improved. In the double grid case, a combination of 90° and 60° angles for each flight allowed us to achieve

the best results for two different overlap configurations. In relation to altitude in the simple grid case, we found that higher altitudes results in a smaller number of points and images, but also reduced precision. In the double grid case we found that most precise reconstruction corresponds to the uses of two specific flight altitudes of $h_1 = 50$m and $h_2 = 150$m.

We also tested the proposed ground segmentation method for forested areas and we were able to reduce the RMSE considerably. This improvement was also reflected in the coverage percentage estimation, where the error has halved. We also performed qualitative analysis using real-world experiments with good results for both tree coverage and height.

The capability to generate the DTM in forested environments using only the point cloud from SfM is the key for UAS-based photogrammetry in cases where there isn't another source available, or is not possible to use LiDAR due to their high cost or operational difficulty. Therefore, the presented method can make UAS-based photogrametry an available tool to a larger set of stakeholders, like local forest management agencies, citizen science and research projects with limited resources.

To summarize we can conclude that UAS-based photogrammetry in forests environments is challenging but still possible and allows to obtain useful results if a proper settings for mission and sensor are considered and an accurate DTM is generated. As demonstrated in this work, it can be used for structural forest parameters estimation and selective logging detection, becoming in a powerful tool for forest inventory and management. In this way we save tedious fieldwork, low-resolution results from satellite imagery and expensive alternatives like airborne LiDAR systems.

Funding: This research was funded by the Agencia Nacional de Promoción Científica y Tecnológica, Argentina and the Ministerio de Ambiente y Desarrollo Sustentable de la Nación, Argentina, under Grant number PICTO-2014-0076.

Data Availability Statement: The data that support the findings of this study are available from the corresponding author upon reasonable request.

Acknowledgments: We also would like to thank the Administración de Parques Nacionales, all park rangers of the Ciervo de los Pantanos national park and specially Luis Paupy for his technical support.

Conflicts of Interest: The authors declare no conflict of interest.The funders had no role in the design of the study; in the collection, analyses, or interpretation of data; in the writing of the manuscript, or in the decision to publish the results. This publication has been approved by all the coauthors, as well as relevant authorities where data acquisition has been carried out.

References

1. McRoberts, R.E.; Tomppo, E.O. Remote sensing support for national forest inventories. *Remote sensing of environment* **2007**, *110*, 412–419.
2. Torresan, C.; Berton, A.; Carotenuto, F.; Di Gennaro, S.F.; Gioli, B.; Matese, A.; Miglietta, F.; Vagnoli, C.; Zaldei, A.; Wallace, L. Forestry applications of UAVs in Europe: A review. *International Journal of Remote Sensing* **2017**, *38*, 2427–2447.
3. Dainelli, R.; Toscano, P.; Di Gennaro, S.F.; Matese, A. Recent advances in unmanned aerial vehicle forest remote sensing—a systematic review. part I: a general framework. *Forests* **2021**, *12*, 327.
4. White, J.C.; Coops, N.C.; Wulder, M.A.; Vastaranta, M.; Hilker, T.; Tompalski, P. Remote sensing technologies for enhancing forest inventories: A review. *Canadian Journal of Remote Sensing* **2016**, *42*, 619–641.
5. Masek, J.G.; Hayes, D.J.; Hughes, M.J.; Healey, S.P.; Turner, D.P. The role of remote sensing in process-scaling studies of managed forest ecosystems. *Forest Ecology and Management* **2015**, *355*, 109–123.
6. Immitzer, M.; Stepper, C.; Böck, S.; Straub, C.; Atzberger, C. Use of WorldView-2 stereo imagery and National Forest Inventory data for wall-to-wall mapping of growing stock. *Forest Ecology and Management* **2016**, *359*, 232–246.
7. Iglhaut, J.; Cabo, C.; Puliti, S.; Piermattei, L.; O'Connor, J.; Rosette, J. Structure from motion photogrammetry in forestry: A review. *Current Forestry Reports* **2019**, *5*, 155–168.
8. Dash, J.P.; Watt, M.S.; Pearse, G.D.; Heaphy, M.; Dungey, H.S. Assessing very high resolution UAV imagery for monitoring forest health during a simulated disease outbreak. *ISPRS Journal of Photogrammetry and Remote Sensing* **2017**, *131*, 1–14.

9. Michez, A.; Piégay, H.; Lisein, J.; Claessens, H.; Lejeune, P. Classification of riparian forest species and health condition using multi-temporal and hyperspatial imagery from unmanned aerial system. *Environmental monitoring and assessment* **2016**, *188*, 146.
10. Lehmann, J.R.K.; Nieberding, F.; Prinz, T.; Knoth, C. Analysis of unmanned aerial system-based CIR images in forestry—A new perspective to monitor pest infestation levels. *Forests* **2015**, *6*, 594–612.
11. Mokroš, M.; Výbošťok, J.; Tomaštík, J.; Grznárová, A.; Valent, P.; Slavík, M.; Merganič, J. High precision individual tree diameter and perimeter estimation from Close-Range photogrammetry. *Forests* **2018**, *9*, 696.
12. Lisein, J.; Michez, A.; Claessens, H.; Lejeune, P. Discrimination of deciduous tree species from time series of unmanned aerial system imagery. *PLoS One* **2015**, *10*.
13. Alonzo, M.; Andersen, H.E.; Morton, D.C.; Cook, B.D. Quantifying boreal forest structure and composition using UAV structure from motion. *Forests* **2018**, *9*, 119.
14. Dainelli, R.; Toscano, P.; Gennaro, S.F.D.; Matese, A. Recent advances in Unmanned Aerial Vehicles forest remote sensing—A systematic review. Part II: Research applications. *Forests* **2021**, *12*, 397.
15. Baltsavias, E.; Gruen, A.; Eisenbeiss, H.; Zhang, L.; Waser, L. High-quality image matching and automated generation of 3D tree models. *International Journal of Remote Sensing* **2008**, *29*, 1243–1259.
16. White, J.C.; Wulder, M.A.; Vastaranta, M.; Coops, N.C.; Pitt, D.; Woods, M. The utility of image-based point clouds for forest inventory: A comparison with airborne laser scanning. *Forests* **2013**, *4*, 518–536.
17. Leberl, F.; Irschara, A.; Pock, T.; Meixner, P.; Gruber, M.; Scholz, S.; Wiechert, A. Point clouds. *Photogrammetric Engineering & Remote Sensing* **2010**, *76*, 1123–1134.
18. Klápště, P.; Urban, R.; Moudrỳ, V. Ground Classification of Uav Image-Based Point Clouds Through Different Algorithms: Open Source vs Commercial Software. *Proceedings of the UAS*, *4*, 4.
19. Pingel, T.; Clarke, K.; Mcbride, W. An Improved Simple Morphological Filter for the Terrain Classification of Airborne LIDAR Data. *ISPRS Journal of Photogrammetry and Remote Sensing* **2013**, *77*, 21–30. doi:10.1016/j.isprsjprs.2012.12.002.
20. Vastaranta, M.; Wulder, M.A.; White, J.C.; Pekkarinen, A.; Tuominen, S.; Ginzler, C.; Kankare, V.; Holopainen, M.; Hyyppä, J.; Hyyppä, H. Airborne laser scanning and digital stereo imagery measures of forest structure: comparative results and implications to forest mapping and inventory update. *Canadian Journal of Remote Sensing* **2013**, *39*, 382–395.
21. Wang, C.; Morgan, G.; Hodgson, M.E. sUAS for 3D Tree Surveying: Comparative Experiments on a Closed-Canopy Earthen Dam. *Forests* **2021**, *12*, 659.
22. Frey, J.; Kovach, K.; Stemmler, S.; Koch, B. UAV photogrammetry of forests as a vulnerable process. A sensitivity analysis for a structure from motion RGB-image pipeline. *Remote Sensing* **2018**, *10*, 912.
23. Ni, W.; Sun, G.; Pang, Y.; Zhang, Z.; Liu, J.; Yang, A.; Wang, Y.; Zhang, D. Mapping three-dimensional structures of forest canopy using UAV stereo imagery: evaluating impacts of forward overlaps and image resolutions with LiDAR data as reference. *IEEE Journal of Selected Topics in Applied Earth Observations and Remote Sensing* **2018**, *11*, 3578–3589.
24. Seifert, E.; Seifert, S.; Vogt, H.; Drew, D.; Van Aardt, J.; Kunneke, A.; Seifert, T. Influence of drone altitude, image overlap, and optical sensor resolution on multi-view reconstruction of forest images. *Remote Sensing* **2019**, *11*, 1252.
25. Fritz, A.; Kattenborn, T.; Koch, B. UAV-based photogrammetric point clouds—Tree stem mapping in open stands in comparison to terrestrial laser scanner point clouds. *Int. Arch. Photogramm. Remote Sens. Spat. Inf. Sci* **2013**, *40*, 141–146.
26. Díaz, G.M.; Mohr-Bell, D.; Garrett, M.; Muñoz, L.; Lencinas, J.D. Customizing unmanned aircraft systems to reduce forest inventory costs: can oblique images substantially improve the 3D reconstruction of the canopy? *International Journal of Remote Sensing* **2020**, *41*, 3480–3510.
27. Nesbit, P.R.; Hugenholtz, C.H. Enhancing uav–sfm 3d model accuracy in high-relief landscapes by incorporating oblique images. *Remote Sensing* **2019**, *11*, 239.
28. Bielova, O.; Hänsch, R.; Ley, A.; Hellwich, O. A Digital Image Processing Pipeline for Modelling of Realistic Noise in Synthetic Images. 2019 IEEE/CVF Conference on Computer Vision and Pattern Recognition Workshops (CVPRW). IEEE, 2019, Vol. tba, p. tba. doi:tba.
29. Koenig, N.; Howard, A. Design and Use Paradigms for Gazebo, An Open-Source Multi-Robot Simulator. IEEE/RSJ International Conference on Intelligent Robots and Systems; , 2004; pp. 2149–2154.
30. Dandois, J.P. Remote sensing of vegetation structure using computer vision. PhD thesis, University of Maryland, Baltimore County, 2014.
31. OpenTopography. National Center for Airborne Laser Mapping (NCALM). *Forests* **2013**. doi:https://doi.org/10.5069/G9V69GJ4.
32. Leachtenauer, J.C.; Driggers, R.G. *Surveillance and reconnaissance imaging systems: modeling and performance prediction*; Artech House, 2001.
33. Cignoni, P.; Rocchini, C.; Scopigno, R. Metro: measuring error on simplified surfaces. Computer graphics forum. Wiley Online Library, 1998, Vol. 17, pp. 167–174.
34. PDAL. PDAL Point Data Abstraction Library, 2018. doi:10.5281/zenodo.2556738.